Histone acetylation increases chromatin accessibility

Sabine M. Görisch[1,*], Malte Wachsmuth[2,‡], Katalin Fejes Tóth[2], Peter Lichter[1] and Karsten Rippe[2,§]

[1]Division of Molecular Genetics, Deutsches Krebsforschungszentrum, Im Neuenheimer Feld 280, 69120 Heidelberg, Germany
[2]Molecular Biophysics Group, Kirchhoff-Institut für Physik, Im Neuenheimer Feld 227, 69120 Heidelberg, Germany
*Present address: Max Delbrück Centre for Molecular Medicine, Wiltbergstr. 50, 13125 Berlin, Germany
‡Present address: Institut Pasteur Korea, 39-1 Hawolgok-dong, Seongbuk-gu, Seoul, 136-791, Korea
§Author for correspondence (e-mail: karsten.rippe@kip.uni-heidelberg.de)

Accepted 12 September 2005
Journal of Cell Science 118, 5825-5834 Published by The Company of Biologists 2005
doi:10.1242/jcs.02689

Summary

In eukaryotes, the interaction of DNA with proteins and supramolecular complexes involved in gene expression is controlled by the dynamic organization of chromatin inasmuch as it defines the DNA accessibility. Here, the nuclear distribution of microinjected fluorescein-labeled dextrans of 42 kDa to 2.5 MDa molecular mass was used to characterize the chromatin accessibility in dependence on histone acetylation. Measurements of the fluorescein-dextran sizes were combined with an image correlation spectroscopy analysis, and three different interphase chromatin condensation states with apparent pore sizes of 16-20 nm, 36-56 nm and 60-100 nm were identified. A reversible change of the chromatin conformation to a uniform 60-100 nm pore size distribution was observed upon increased histone acetylation. This result identifies histone acetylation as a central factor in the dynamic regulation of chromatin accessibility during interphase. In mitotic chromosomes, the chromatin exclusion limit was 10-20 nm and independent of the histone acetylation state.

Key words: Heterochromatin, Image correlation spectroscopy, Trichostatin A, Microinjection

Introduction

The higher order chromatin structure is an important regulatory mechanism of gene expression and can be classified into two cytologically distinct conformations: relatively uncondensed euchromatin and much denser chromatin regions referred to as heterochromatin (Heitz, 1928). Heterochromatin is transcriptionally less active than euchromatin. Regions of so called facultative heterochromatin can display a transition to a more open, transcriptionally active conformation, which is characterized by its higher accessibility to DNase I or micrococcal nuclease (Bellard et al., 1980; Dillon, 2004; Dillon and Festenstein, 2002; Gilbert et al., 2004; van Holde, 1989; Weintraub and Groudine, 1976; Wu et al., 1979). According to present knowledge (Dillon, 2004; Maison and Almouzni, 2004), heterochromatic regions in mammalian cells are characterized by the following features: (1) a higher DNA density and an increased AT base pair content as apparent upon staining the DNA with Hoechst 33258 or 4′-6-Diamidino-2-phenylindole (DAPI) (Zimmer and Wahnert, 1986); (2) tri-methylation at lysine 9 of histone H3 (tri-H3-K9) and lysine 20 of histone H4 (tri-H4-K20) (Lachner et al., 2003; Peters and Schubeler, 2005; Zinner et al., 2005); (3) a preferential binding of HP1α and HP1β (Maison and Almouzni, 2004; Minc et al., 1999; Nielsen et al., 2001); and (4) a decreased level of histone H3 and H4 acetylation (Jeppesen et al., 1992; Jiang et al., 2004; Johnson et al., 1998).

From a number of studies it has been concluded that histone acetylation is essential for the establishment of a transcriptionally competent state of chromatin (Kadonaga, 1998; Roh et al., 2005; Strahl and Allis, 2000; Tse et al., 1998; Zhang et al., 1998). The histone acetylation level can be increased by inhibition of histone deacetylases with low molecular mass compounds like Trichostatin A (TSA) allowing the in vivo analysis of the effect of histone acetylation on chromatin conformation and gene expression as reported in a number of studies. The previously reported effects of TSA treatment include the formation of a stable hyperacetylated and transcriptionally active state of centromeric chromatin in *S. pombe* (Ekwall et al., 1997), a relocation of centromeres to the nuclear periphery in a mouse cell line (Taddei et al., 2001), the distribution of heterochromatin marker protein HP1 in the nucleus (Maison et al., 2002), and a reversible chromatin decondensation up to the micrometer scale in HeLa cells (Fejes Tóth et al., 2004).

It is frequently postulated that the induction of a more ‘open’ chromatin state in response to histone acetylation increases the accessibility of transcription complexes to genomic DNA and that this is an important factor for the regulation of gene expression. However, experimental evidence for this concept is missing. This issue is addressed here by measuring the local accessibility of chromatin directly from the nuclear distribution of fluorescent dextrans with different sizes. In previous studies, a mostly unlimited nuclear access has been reported for a dextran size of 77 kDa and a protein size of 600 kDa (Görisch et al., 2005; Görisch et al., 2003; Verschure et al., 2003). By contrast, the dextran distribution became increasingly restricted for a dextran size of 148 kDa and dextrans of 464 kDa were clearly excluded from putative heterochromatic regions (Görisch et al., 2003).

In this report, the effect of histone acetylation on the size-dependent accessibility of chromatin was examined by nuclear microinjection of dextrans from 42 kDa to 2.5 MDa molecular mass labeled with fluorescein isothiocyanate (FITC-dextrans). Different chromatin conformation states and a striking increase

of accessibility in response to histone acetylation were detected. The results have a number of implications for the regulation of gene expression via modulating the chromatin accessibility to modifying complexes and the transcription machinery.

Materials and Methods

Cell culture and microinjection

HeLa cells (ATCC: CCL-2) were cultured on glass coverslips for fixed cell analysis and on MatTek glass bottom dishes (MatTek, Ashland, MA) for in vivo imaging in DMEM for 1 day. Solutions of 42, 77, 148, 282, 464 and 2500 kDa FITC-dextrans (Sigma, Munich, Germany) at 2% (w/v) concentration with sizes according to lot analysis were used for microinjection as described previously (Görisch et al., 2003). For TSA treatment, cells were cultured for 6 hours after microinjection and than incubated with 100 or 200 ng/ml TSA (Sigma-Aldrich, St Louis, MO) for 17 hours. Cells were fixed in 4% formaldehyde with 2% sucrose for 30 minutes on ice. Coverslips were mounted using Vectrashield with 4′-6-Diamidino-2-phenylindole (DAPI) (Vector, Burlingame, CA). For in vivo staining of the chromatin, cells were cultured using DMEM without phenol red and incubated with 1 μg/ml Hoechst 33258 (Molecular Probes, Leiden, NL) for 20 minutes prior to image acquisition. The H2A-YFP-expressing HeLa cells were grown as described (Fejes Tóth et al., 2004).

Fluorescence microscopy

Three-dimensional stacks of fixed cells were acquired with the Leica TCS SP2 confocal laser scanning microscope (Leica Microsystems, Mannheim, Germany) using a 63×/1.32 NA oil immersion objective. A diode and an Argon laser were used for DAPI (λ=405 nm), FITC (λ=488 nm) and YFP (λ=514 nm) excitation. For the two-color analysis a sequential image acquisition with emission detection from 410-470 nm (DAPI or Hoechst 33258) and at 492-555 nm (FITC) was used in order to avoid crosstalk between the two different signals. The YFP emission was detected at 526-600 nm. For the analysis of the reversibility of the TSA-induced accessibility changes, living cells were imaged before, during and after TSA treatment with Hoechst 33258 chromatin staining. The kinetics of the chromatin decondensation by TSA were determined by in vivo recording the H2A-YFP fluorescence image of HeLa cells over a time period of 3 hours.

Fluorescence correlation spectroscopy (FCS)

The diffusion coefficient D of dextrans in water was determined from FCS measurements acquired with the Leica TCS SP2 FCS2 system and a 63×/1.2 NA water immersion objective. The diffusion correlation time was measured in aqueous solution at 27°C and converted into D by using a 59 bp DNA duplex with a D at 20°C in water of $D_{20,w}$=5.3·10^{-7} cm^2 s^{-1} as reference sample (Rippe et al., 1998). From D the radius of gyration R_G was calculated according to

$$R_G = 1.504 \cdot \frac{kT}{6\pi\eta D}, \quad (1)$$

with η being the viscosity. The radius of gyration R_G describes the dimensions of random coil particles like the FITC-dextrans (Lukacs et al., 2000; Seksek et al., 1997). The R_G value of a random coil is approximately equivalent to the radius r of a much more rigid spherical protein. A corresponding protein molecular mass M can be calculated according to Eqn 2

$$M = \frac{4}{3} \cdot \pi \cdot r^3 \frac{N_A}{\bar{v}}, \quad (2)$$

where the average value of the partial specific protein volume is $\bar{v}$ = 0.73 ml g^{-1} and N_A is the Avogadro number 6.022·10^{23} mol^{-1} as described previously (Görisch et al., 2005).

Image correlation spectroscopy

The typical length of spatial density fluctuations and their amplitude for dextrans and DNA were determined by calculating the radial spatial correlation function of pixel intensities from the CLSM images. Only intensities from pixels in the nuclei were taken. Based on the 2D correlation function according to

$$G_{kl}(\Delta x,\Delta y) = \frac{\langle I(x+\Delta x,y+\Delta y)\, I(x,y)\rangle}{\langle I(x,y)\rangle^2} - 1 . \quad (3)$$

For a review of image correlation spectroscopy (ICS) theory and applications, see Petersen (Petersen, 2001). The radial correlation function $G_{kl}(r)$ was computed by averaging over all displacements in x and y direction with

$$r = \sqrt{\Delta x^2 + \Delta y^2} .$$

The resulting spectra were fitted with Gaussian functions using Origin (OriginLab, Northampton, MA, USA). The half width at half maximum of the shortest decay in the chromatin correlation function was identified as the correlation length l. The amplitude of the correlation function was taken from the fit in order to correct for potentially autocorrelated single pixel noise. For k=l, Eqn 3 yields the autocorrelation function G, which was computed for both the chromatin distribution from the DAPI fluorescence signal, $G_1(r)$, and for the differently sized dextrans from the FITC fluorescence signal referred to as $G_2(r)$. From the correlation length l_c of chromatin subcompartments, the TSA-dependent condensation state of chromatin was derived as described previously from three adjacent layers per cell for 19 cells (Fejes Tóth et al., 2004). To determine the co-localization/exclusion between dextrans and chromatin, the cross-correlation function $G_x(r)$ between the DAPI and the FITC signal was computed according to Eqn 3 with k=1 and l=2, and normalized for intensity differences by the geometric mean of both autocorrelation function amplitudes according to Eqn 4.

$$ratioG(r) = \frac{G_\times(r)}{\sqrt{G_1(0)\cdot G_2(0)}} . \quad (4)$$

The resulting function $ratioG$(r) yields the correlation coefficient $ratioG_0$=$ratioG$(0) at r=0, from which the co-localization ($ratioG_0$>0) or exclusion ($ratioG_0$<0) of dextrans and chromatin were obtained. In addition, a cross-correlation length l_x was determined to describe the length, on which co-localization or exclusion was observed.

The data for the dependence of $ratioG_0$ on the radius of gyration R_g of the different dextrans were fit with the empirically derived relation

$$\mathrm{ratio}G_0(R_G) = \frac{q}{1+\exp\left(\frac{R_G - r_1}{w_1}\right)} + \frac{1-q}{1+\exp\left(\frac{R_G - r_2}{w_2}\right)} + p - 1 . \quad (5)$$

In Eqn 5, r_1 and r_2 describe the R_G values, where the chromatin accessibility changes with the width of the transition given by w_1 and w_2. The relative contribution of the two characteristic radii is given by q. The parameter p represents the value for the correlation coefficient $ratioG_0$ for very small molecules that approach the limit of $R_G \to 0$. An apparent pore size d can be related to the molar

nucleosome concentration c according to Eqn 6 as described (Weidemann et al., 2003).

$$d(c) = 30\ \text{nm} \cdot \left(\frac{c}{1.16\ \text{mM}} \right)^{\frac{1}{2}} - 30\ \text{nm}\ . \qquad (6)$$

The nucleosome concentration of 1.16 mM is the concentration for a hexagonal dense packaging of 30 nm diameter cylinders and constitutes the approximate upper limit estimate for a concentration that can be obtained when the 30 nm fiber structure is maintained.

Results

TSA-induced histone acetylation increases chromatin accessibility

FITC-labeled dextrans of 42, 77, 148, 282, 464 and 2500 kDa molecular mass were microinjected into HeLa cell nuclei. The DNA was counterstained with DAPI to allow a comparison of the FITC signal with the chromatin distribution. Regions with intense DAPI staining represent bona fide heterochromatin, while the more open euchromatin displays a weaker DAPI fluorescence. As observed previously, small dextrans were homogeneously distributed, while the large dextrans accumulated in certain regions of the nucleus (Görisch et al., 2003). The distribution of dextrans and chromatin can be qualitatively compared via the linescans shown in Fig. 1. The 42 (Fig. 1A) and the 77 kDa dextrans (Fig. 1B) had access to both euchromatic and heterochromatic regions. The 282 kDa (Fig. 1C) and the 464 kDa dextrans (Fig. 1D) were mostly excluded from the heterochromatin at the nuclear periphery and around the nucleoli. The 2.5 MDa dextrans were excluded also from the low-density chromatin regions and restricted to a few small patches (Fig. 1E). An inspection of multiple linescans shows that there is some overlap mostly at peripheral regions of the 2.5 MDa dextran patches with chromatin-associated fluorescence. This can be explained by the polymer properties of both dextrans and chromatin, which allow the macromolecules to intermingle slightly. However, the overall exclusion of the larger 2.5 MDa dextrans from chromatin is obvious at the regions of higher dextran concentrations. This is also evident on electron micrographs reported earlier (Görisch et al., 2003). To determine how acetylation-induced chromatin rearrangements affect the accessibility of chromatin, the microinjected cells were treated with TSA for 17 hours. Under these conditions a significant increase of mono-, di-, tri- and tetra-acetylated histone H4 was visible on triton acid urea gels (data not shown) as described previously (Hoshikawa et al., 1994; Niki et al., 1999), demonstrating that histones were hyperacetylated.

Upon TSA treatment, the nuclear distributions of the 42 (Fig. 1A) and the 77 kDa (Fig. 1B) dextrans appeared to be unchanged while the 282 and 464 kDa dextrans gained access to previously heterochromatic areas that decondensed upon histone acetylation (Fig. 1C). Notably, the distribution of the 464 kDa dextrans in TSA-treated cells was similar to that of the 77 kDa

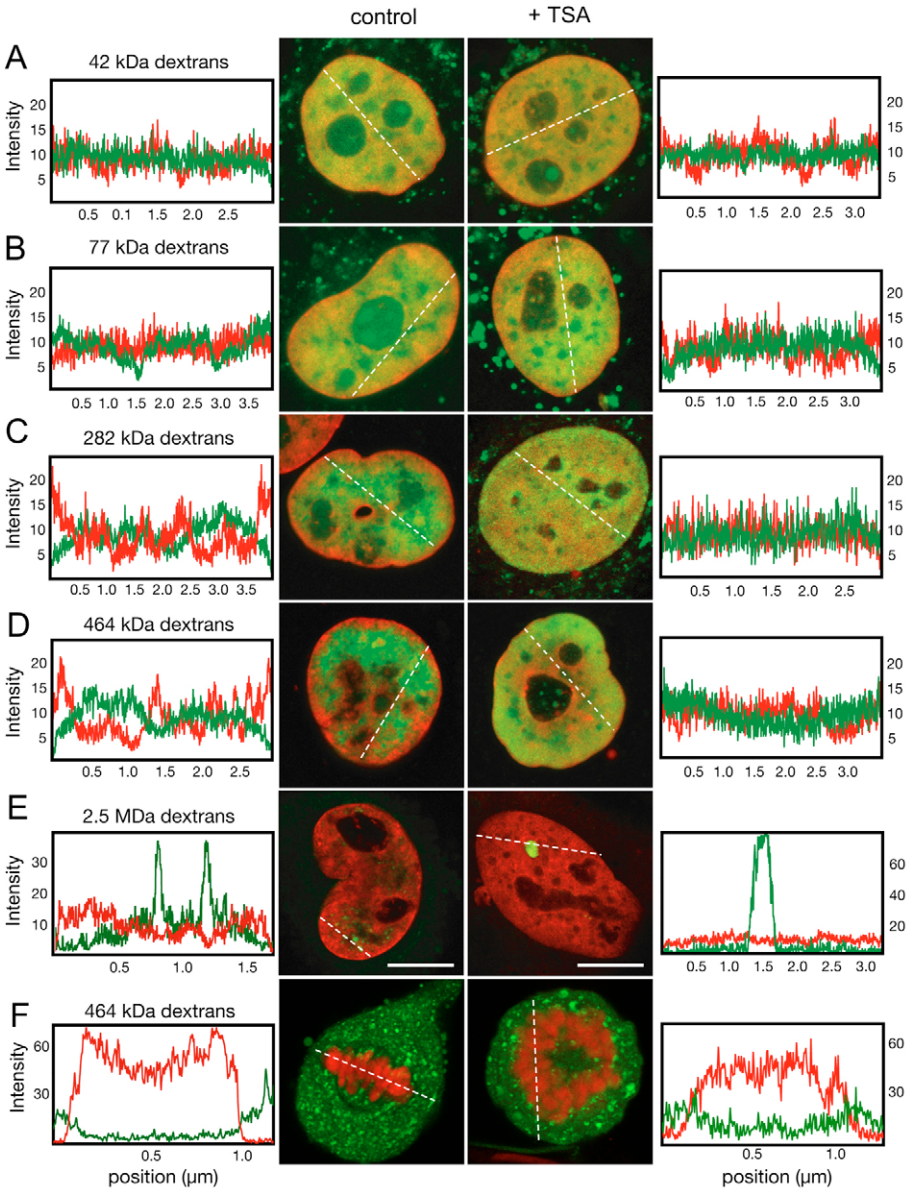

Fig. 1. TSA-induced increase in chromatin accessibility. Examples of confocal sections of HeLa interphase cell nuclei (A-E) microinjected with 42, 77, 282, 464 and 2500 kDa and of mitotic cells microinjected with 464 kDa FITC-dextrans (F) are presented. The dextran signal is in green and the DNA counterstained with DAPI is in red. The left side shows control cells and the right side cells after 17 hours of TSA treatment. The dashed lines indicate the direction of the corresponding linescans that are shown next to the images. Scale bars, 10 μm.

dextrans in untreated cells. By contrast, the 2.5 MDa dextrans did not show increased chromatin accessibility after TSA treatment, but were confined to a reduced number of globular accumulations (Fig. 1E). Typically, only one or two larger accumulations were detected in TSA-treated cells as opposed to a larger number of smaller patches in the control cells.

The change of chromatin accessibility due to TSA treatment correlates with the decondensation kinetics and is reversible

The change of chromatin accessibility for dextrans due to TSA-induced acetylation was also studied in vivo to analyze the reversibility and the time scale of the changes. Before TSA treatment, the living cells showed essentially the same 464 kDa dextran-to-chromatin distribution as observed in fixed cells (compare Fig. 1D to Fig. 2A). Already after 3-4 hours of incubation with TSA, the access of the dextrans to previously dense chromatin regions increased significantly (Fig. 2A, top panel). The maximum effect required TSA treatment for >10 hours (Fig. 2A, bottom panel). Changes in accessibility were reversible upon washing out the TSA. Exclusion from heterochromatic regions was visible again 3-4 hours after removal of TSA (Fig. 2A).

The kinetics of the accessibility changes followed the kinetics of the chromatin decondensation, which is quantified in Fig. 2B. As a parameter that reflects the chromatin condensation state, the chromatin correlation length was determined at each time point. From the fit of a single-exponential reaction kinetic to the data, a half-time of $t_{1/2}\approx 3.5$ hours was obtained (Fig. 2B).

The physical dimensions of the FITC-dextrans combined with an image correlation spectroscopy analysis yield apparent chromatin pore sizes

To correlate the observed dextran distributions with the folding of chromatin in the nucleus, the dimensions of the dextrans were determined from in vitro measurements by fluorescence correlation spectroscopy (FCS). Using the dextrans as molecular rulers, their relative distribution with respect to chromatin was quantified by image correlation and cross-correlation spectroscopy.

Dextrans are polymers, which adopt a dynamic random coil conformation. The size of such particles can be described by their radii of gyration R_G (Lukacs et al., 2000; Seksek et al., 1997), which characterizes the average distance of monomeric units from the center of mass of the molecule. The corresponding diameter (2 R_G) serves as a good estimate for the minimal pore size of the microenvironment, to which a given molecule has access (Lénárt et al., 2003). Here, the radius of gyration of the dextrans was determined from in vitro measurements of their diffusion coefficients D by fluorescence correlation spectroscopy according to Eqn 1 (Fig. 3E). From the known apparent diameter of the dextrans, the mean pore size d of those regions was determined, into which dextrans of a certain size could still intrude (Table 1).

The chromatin accessibility for dextrans in the nucleus was quantified by image cross-correlation spectroscopy. The cross-correlation coefficient $ratioG_0$ describes the co-localization of

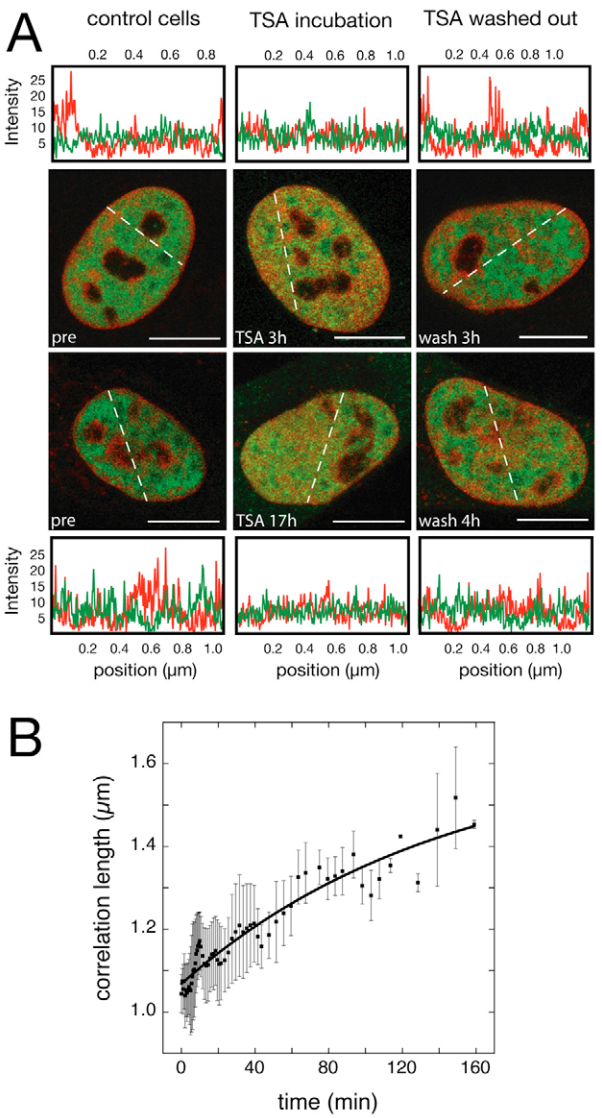

Fig. 2. Reversibility of chromatin accessibility changes due to hyperacetylation. (A) Time series of HeLa cell nuclei with microinjected 464 kDa dextrans (green) and Hoechst DNA stain (red) before TSA treatment, after 3 or 17 hours TSA incubation and 3 or 4 hours after removal of TSA. The dashed lines indicate the direction of the corresponding linescans, which are shown adjacent to the images. Scale bars, 10 μm. (B) Kinetics of chromatin decondensation due to TSA-induced histone acetylation. The increase of the chromatin correlation length represents the induced decondensation. The fit curve is a single-exponential reaction kinetics with a half-time of 3.5 hours.

dextrans and chromatin with values of 1 representing perfect co-localization, of ~0 for no correlation, and of –1 for complete mutual exclusion of the two distributions. The nucleus contains a number of subnuclear organelles like PML and Cajal bodies or SC35 speckles, which exclude both dextrans and chromatin. Accordingly, a completely uncorrelated distribution of chromatin and FITC-dextrans would not yield exactly a $ratioG_0$=0 but rather a slightly positive value around 0.13 for the TSA-treated and 0.19 for the control cells in this study. Thus, a value of $ratioG_0$=0.00±0.02 determined for the 77 kDa

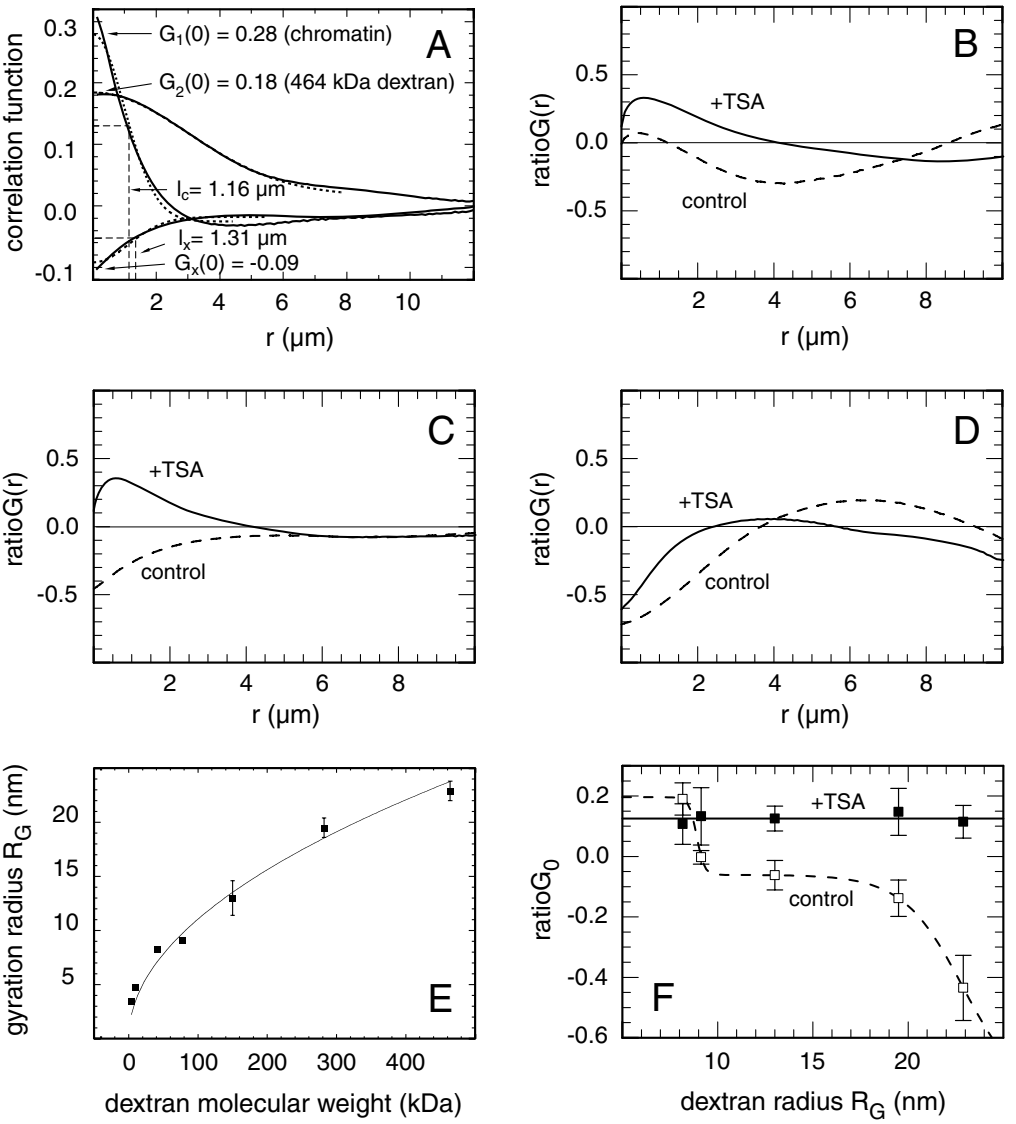

Fig. 3. Image cross-correlation spectroscopy analysis of dextran and chromatin distribution. (A) Example of the image correlation spectroscopy analysis of cells, into which 464 kDa FITC-dextrans were injected. The autocorrelation function of the DAPI-stained chromatin distribution, $G_1(r)$, and of the distribution of the 464 kDa FITC-dextrans, $G_2(r)$, as well as the cross-correlation function of the two distributions, $G_x(r)$, were computed as described in the text (Eqn 3). The dashed lines are Gaussian fits to the shortest decay of each correlation function, from which the autocorrelation amplitudes $G_1(0)$ and $G_2(0)$ are obtained as indicated. These values are then used to calculate the normalized cross-correlation function *ratioG*(r) with its value at r=0, *ratio*G_0, according to Eqn 4. This normalizes for intensity differences between images. The autocorrelation length l_c that describes the chromatin condensation state is the length, after which the Gaussian fit to the DAPI-stained chromatin correlation function has decreased to half of its maximum value. Due to the exclusion of the dextrans from condensed chromatin areas, the cross-correlation curve and its Gaussian fit have a negative amplitude $G_x(0)$. From the decay of the $G_x(r)$ curve, the cross-correlation length l_x for the exclusion is determined in analogy to the autocorrelation length. (B-D) Normalized cross-correlation curves for dextrans in control (broken line) and TSA-treated cells (solid line). (B) 77 kDa dextran during interphase. (C) 464 kDa during interphase. (D) 464 kDa dextrans during metaphase. (E) Measured dextran sizes given by the radius of gyration R_G. As expected for a random coil, R_G is proportional to the square root of the dextran mass m and a very good fit (solid line) to the expression R_G=1.104 nm kDa$^{-1/2}$ $m^{1/2}$ was obtained. Error bars for the low molecular mass dextrans are smaller than the size of the data points. (F) Nuclear distribution of dextrans with respect to chromatin in dependence of dextran size for control (broken line) and TSA-treated cells (solid line) during interphase. The co-localization/exclusion of dextrans from chromatin is expressed as the normalized cross-correlation signal *ratio*G_0 according to Eqn 3. Eqn 4 was fit to the data for the control cells (broken line) with values of r_1=8.9 nm and r_2=22.9 nm. For the TSA-treated cells a constant line (solid line) with the average value of *ratio*G_0 is depicted.

dextrans already indicates exclusion from certain nuclear subcompartments.

Crosstalk between detection channels leads to a global increase of *ratio*G_0, but was avoided in this study by using sequential scanning. Chromatic aberrations would result in a spatial shift between different channels and a subsequent decreased maximum *ratio*G_0<1 as well as an increased minimum *ratio*G_0>–1, i.e. the range from positive to negative correlations is reduced to a smaller interval. As our analysis was not based on the absolute *ratio*G_0 values but on their differences any chromatic aberration would only lead to a loss of resolution in the accessibility pattern. For the microscopy system used here, the chromatic shift was around 100 nm and well below the shortest correlation length. On simulated images we found that under these conditions the *ratio*G_0 values change by less than 10%.

From the shape of the *ratioG*(r) function, a characteristic cross-correlation length l_x is derived and describes the average size of regions, in which dextrans and chromatin are co-localized or mutually excluded (Fig. 3). Average values for the relative distribution of all dextrans with respect to chromatin are summarized in Table 2 with examples for normalized image cross-correlation curves *ratioG*(r) depicted in Fig. 3B-D. The computation of *ratio*G_0 and the cross-correlation length l_x allows a quantitative comparison of the dextran distributions in dependence of dextran mass. These molecular masses can be

Table 1. Diffusion coefficients and physical dimensions of dextrans

Dextran (kDa)	$D_{20,w}$ ($\mu m^2\ s^{-1}$)*	R_G (nm)†	R_G from fit (nm)‡	Apparent pore size d (nm)‡	Nucleosome concentration (mM)§
4	95.6±2.4	3.4±0.1	2.3	5	0.90
10	67.9±1.0	4.7±0.1	3.5	7	0.76
42	39.4±0.4	8.2±0.1	7.1	14	0.54
77	35.2±0.6	9.1±0.1	9.7	19	0.44
148	24.7±3.1	13.0±1.6	13.4	27	0.32
282	16.6±0.8	19.5±0.9	18.5	37	0.23
464	14.0±0.6	22.9±5.1	23.7	48	0.18
2500¶	ND	ND	~55¶	~110¶	0.05

*Diffusion coefficients (D) measured by fluorescence correlation spectroscopy (FCS) were corrected to 20°C in water.

†R_G is the radius of gyration calculated from the measured D according to Eqn 1.

‡As expected for a random coil, R_G was proportional to the square root of m yielding an excellent fit to the expression R_G=1.104 nm $kDa^{-1/2}$ $m^{1/2}$ as shown in Fig. 3E. An averaged value of R_G was derived from the fit corresponding to an accessible pore diameter d=2·R_G through which a dextran of a certain size can still translocate.

§The apparent pore size was converted to nucleosome concentration according to Eqn 6, which assumes a regular spacing of 30 nm chromatin fibers.

¶The D of the 2500 kDa dextran could not be measured by FCS because, owing to its slow mobility, a significant amount of bleaching occurred during its dwell time in the focus. The value of 110 nm was derived from extrapolation of the fit curve.

ND, not determined.

assigned to the calculated dextran diameters as listed in Table 1 to determine the physical dimensions of the accessible regions in the chromatin fiber network.

Chromatin adopts at least three different condensation states with respect to its accessibility for macromolecules

The 464 kDa particles with a diameter of 47 nm are excluded from the dense chromatin at the nuclear periphery and the nucleolus, but can still access the less denser central chromatin regions (Fig. 1D, Fig. 3C, Table 2). By contrast, the larger 2.5 MDa dextrans (d ~110 nm) are excluded from chromatin, i.e. they are trapped by the chromatin network at sites, where they were probably injected and from which they cannot escape by diffusion. The observed exclusion of the 2.5 MDa dextrans is in good agreement with the observation that 2 MDa dextrans are essentially immobile in the nucleus (Seksek et al., 1997) and that 100 nm sized microspheres display strongly restricted movements with fast translocations of the center-of-mass confined to a corral with a radius of 150 nm (Tseng et al., 2004). Thus, the upper limit for the maximal pore size of open euchromatin regions is around 100 nm.

Based on the dependence of *ratio*G_0 on the dextran radius of gyration in the control cells, a fit curve according to Eqn 5 was obtained that is indicative of two additional exclusion sizes. These are characterized by radius r_1=9±1 nm and r_2=23±5 nm (Fig. 3F, open squares). The corresponding chromatin pore sizes of two times the gyration radii are d_1=16-20 nm and d_2=36-56 nm. The value of d_1 reflects the observation that some exclusion from certain regions is detected already for the 77 kDa dextrans with 20 nm diameter. A second transition for the accessibility takes place at a radius of gyration of r_2=23±5 nm and represents the radius limit for particles, which are excluded from condensed chromatin regions with a corresponding pore size of d_2=36-56 nm. However, particles in this range like the 282 kDa and 464 kDa dextrans can still access open chromatin regions, which accordingly need to have a pore size of at least 60 nm. With the upper limit given by the exclusion of the 2.5 MDa dextrans and 100 nm microspheres (Tseng et al., 2004) from chromatin, a value of d_3=60-100 nm can be estimated for the pore size of the relatively uncondensed euchromatin in the central regions of the nucleus. All areas accessible to larger molecules and complexes, like for example the 2.5 MDa dextrans or Cajal or PML nuclear bodies, have obviously a pore size larger than 100 nm. However, these regions are topologically not connected anymore and can be referred to as interchromatin space. Accordingly, the movement of particles of >100 nm size within the nucleus over larger distances requires a translocation of the surrounding chromatin 'corral' as discussed previously (Görisch et al., 2005; Görisch et al., 2004).

It should be noted that with the combination of specific fluorescence labeling of chromatin and dextrans and two-color cross-correlation used here, only the chromatin contribution to dextran exclusion and accessibility is assessed. Additional

Table 2. Correlation coefficients and correlation lengths for FITC-dextrans and chromatin

	Control			TSA		
Dextran (kDa)	*ratio*G_0*	l_x (μm)†	l_c (μm)‡	*ratio*G_0*	l_x (μm)†	l_c (μm)‡
Interphase						
42	0.19±0.05	1.77±0.02	1.3±0.1 (average)	0.11±0.07	2.0±0.4 (average)	1.8±0.1 (average)
77	0.00±0.02	ND		0.13±0.09		
148	–0.06±0.05	ND		0.13±0.04		
282	–0.14±0.06	0.27±0.02		0.15±0.08		
464	–0.43±0.11	1.26±0.04		0.11±0.05		
Metaphase						
77–2500§	–0.59±0.08	1.80±0.62	1.6±0.3	–0.67±0.06	1.8±0.7	3.4±0.1

*The *ratio*G_0 value is the normalized cross-correlation coefficient according to Eqn 4.

†l_x is the cross-correlation length on which dextrans and chromatin were co-localized (*ratio*G_0>0.1) or mutually excluded (*ratio*G_0<0.1). In the case of –0.1<*ratio*G_0<0.1, the value of l_x was too small and could not be reliably determined as indicated (ND). Values of l_x for TSA are averages as no dependence on dextran size was observed.

‡l_c is the correlation length of chromatin determined from the autocorrelation function of the DAPI signal. The chromatin distribution was not affected by the size of dextrans injected and values were averaged for all cells.

§Dextrans of 77-, 464- and 2500-kDa were indistinguishable in their distribution during metaphase and values were averaged.

fluctuations of the dextran distribution due to nuclear components not (cor-)related to chromatin are disregarded. Three different cases for the influence of non-chromatin components can be distinguished. First, they can be freely mobile and therefore do not lead to a sustainable exclusion from specific loci. Second, they can be so large, like for example nuclear PML or Cajal bodies, that chromatin is also excluded from them. In this case they do not contribute to a possible anticorrelation but they lead to a dextran size-independent positive contribution to the correlation function. Third, they could be chromatin-associated. Then their impact on the dextran distribution is chromatin-correlated, and they contribute to the effective chromatin porosity, although they are not directly visualized.

Interestingly, the mitotic chromosomes were found to be completely inaccessible to the dextrans studied in the range of 77-2500 kDa, and no size effect was detected with an average $ratioG_0$=–0.59±0.08 (Fig. 1F, Table 2). This demonstrates that the pore size during metaphase has to be below ~20 nm, which would be the size of the 77 kDa dextrans. As reported previously, smaller transcription factors and chromosomal proteins like UBF, H1, RPA43 and TBP in the size of up to 10 nm diameter [UBF dimer (Neil et al., 1996)] have access to mitotic chromosomes (Chen et al., 2005). Thus, an apparent pore size of 10-20 nm can be estimated for chromatin condensed into mitotic chromosomes.

Hyperacetylated chromatin decondenses to a uniform chromatin conformation with an apparent pore size of 60-100 nm

In interphase cells, the TSA-induced histone acetylation led to an increase of the chromatin correlation length l_c from 1.3±0.1 μm to 1.8±0.1 μm. The value of l_c was determined from the autocorrelation of the DAPI images $G_1(r)$ and describes the size of chromatin substructures with similar density (Table 2, Fig. 3A). Its increase reflects the disintegration of dense chromatin regions and the transition to a more homogeneous chromatin distribution as described previously (Fejes Tóth et al., 2004).

The decondensation of heterochromatic regions at the nuclear periphery and around the nucleolus was accompanied by increased chromatin accessibility, which was most striking for the 464 kDa FITC-dextrans (d ~ 46 nm). The strong exclusion of these particles from dense chromatin regions with $ratioG_0$=–0.43±0.11 observed in the control cells disappeared completely upon TSA treatment, where a value of $ratioG_0$=0.11±0.05 was determined. Upon increased histone acetylation, the dextran distribution became virtually independent of molecular mass in the range from 42 to 464 kDa with values of $ratioG_0$ between 0.11 and 0.15 (Table 2, Fig. 3F closed squares). Only the 2.5 MDa FITC-dextrans, for which a pore size of >110 nm is required for accessibility (Table 1), remained excluded from chromatin. This demonstrates that upon hyperacetylation, the chromatin regions with apparent pore sizes of d_1=16-20 nm and d_2=36-56 nm decondensed to an average pore size of 60-100 nm. Interestingly, the nuclear dextran patches formed by the 2.5 MDa dextrans became larger, round and more confined upon incubation with TSA (Fig. 1E). This suggests that the chromatin decondensation decreases the interchromatin space available to molecules of this size so that a more confined distribution is present.

For the mitotic chromosomes, the TSA treatment had no significant effects on the accessibility of dextrans in the size range of 77-2500 kDa. Thus, the chromatin pore size remained below 20 nm as in the control cells. However, a strong increase in the chromatin correlation length from 1.6±0.3 μm to 3.4±0.1 μm was measured (Table 2). On the DAPI images, it is apparent that the outline of the chromosomes in control cells is well defined, while in the TSA-treated mitotic cells the contours were fuzzy and the chromosomes looked swollen with hardly any fluctuations of the chromatin density (Fig. 1F). This suggests that even for mitotic chromosomes, some chromatin decondensation was induced in response to histone hyperacetylation. However, these structural changes did not increase the accessibility of mitotic chromatin for the dextrans studied.

Discussion

Here we have demonstrated that histone acetylation increases chromatin accessibility by measuring the size-dependent nuclear distribution of microinjected FITC-dextrans in combination with an image correlation spectroscopy analysis. This allowed the description of the dynamic accessibility of different chromatin states in response to histone acetylation with an apparent pore diameter, which defines the maximal size of complexes capable to penetrate these regions.

In interphase cells, three different chromatin condensation states were identified as illustrated in Fig. 4. For putative open euchromatin regions in the nuclear center, an apparent pore size of 60-100 nm was calculated, because here only the 2.5 MDa dextrans were excluded from most of the chromatin. This is also evident on electron micrographs reported earlier (Görisch et al., 2003) and consistent with the following two observations: 2 MDa dextrans are essentially immobile in the nucleus (Seksek et al., 1997) and 100 nm sized microspheres display strongly restricted movements with fast translocations of the center-of-mass confined to a corral with a radius of 150 nm (Tseng et al., 2004).

The 282 and 464 kDa dextrans were excluded from perinuclear and perinucleolar heterochromatin, as can be seen directly in the images, and an apparent pore size of 36-56 nm was determined. The exclusion occurs on the μm length scale as quantified by the cross-correlation length of l_x=0.27±0.02 μm (282 kDa dextrans) and l_x=1.26±0.04 μm (464 kDa dextrans), consistent with the extension of these regions on the images (Fig. 1, Table 2). Furthermore, an additional particularly dense chromatin compaction state with a 16-20 nm exclusion limit was identified here, which could reflect the existence of functionally distinct conformations as for example centromeric or telomeric heterochromatin, or heterochromatin formed with other repetitive sequences. The nuclear localization of this highest chromatin condensation state is unclear and subject of a study in progress applying a spatially resolved correlation analysis. An analysis of an intensity threshold-dependent pixel distribution suggests that these loci are also predominantly present at the nuclear and nucleolar periphery inasmuch as they are likely to be found in regions with the highest DAPI signal. This is indicated in Fig. 4.

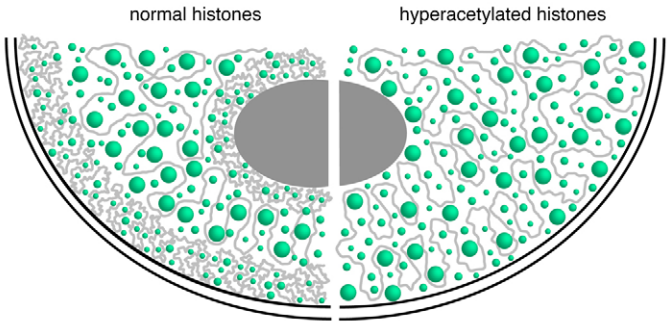

Fig. 4. Illustration of chromatin accessibility. The chromatin is shown in gray and macromolecules are represented by three differently sized spheres in green corresponding to the distribution of 42, 77 and 464 kDa dextrans. The left side illustrates an untreated cell, where small molecules can diffuse in all parts of the chromatin with a subfraction of heterochromatin being accessible only to the smallest particles. The large complexes are excluded from heterochromatin and restricted to more open chromatin regions in the nuclear center. The right side shows schematically the macromolecule distribution in a TSA-treated cell. The dense chromatin regions are disintegrated so that also the large complexes can distribute throughout the complete nucleus.

When a regular spacing of the 30 nm chromatin fiber is assumed, the apparent pore sizes measured here can be converted into nucleosome concentrations according to Eqn 6 (Table 1) (Weidemann et al., 2003). The resulting values for euchromatin with 0.06-0.13 mM (60-100 nm pore size) and the bulk heterochromatin 0.14-0.24 mM (36-56 nm pore size) are in good agreement with the measured average nucleosome concentration in HeLa nuclei of 0.14±0.03 mM for bulk chromatin and 0.2-0.3 mM for dense chromatin regions (Weidemann et al., 2003). The high-density heterochromatin (16-20 nm pore size) would correspond to a nucleosome concentration of 0.4-0.5 mM.

The apparent pore size can be related to the diameter of globular proteins able to access a corresponding chromatin subcompartment (see Eqn 2) (Görisch et al., 2005). Up to a diameter of 14 nm (42 kDa dextrans) corresponding to a molecular mass of a ~1 MDa globular protein, we did not detect any limitation in access to chromatin. This is also consistent with the observations that a ~600 kDa RNA polymerase-GFP construct is homogenously distributed throughout the nucleus (Verschure et al., 2003) and that small sequence-specific regulatory proteins are able to bind to their target sites in heterochromatin (Chen and Widom, 2004). Conversely, complexes in the 2-3 MDa range like the RNA polymerase II holoenzyme complex (Yankulov et al., 1999) or the SWI/SNF chromatin remodeling complex (Smith et al., 2003) correspond in size to the 77 kDa dextrans and would experience some local exclusion from the densest chromatin regions with 16-20 nm pore size. In this context, it is noteworthy that in the case of the SWI/SNF complex, histone acetylation could have a dual role: it could facilitate the access of SWI/SNF to a certain genomic locus and at the same time provide a recognition site for its bromodomain subunit, which mediates stable binding to acetylated histones (Agalioti et al., 2002; Hassan et al., 2002).

The bulk heterochromatin with an apparent pore size of 36-56 nm would not restrict the access of multi-subunit protein complexes in the size of several MDa to these regions. However, it might be relevant for larger supramolecular complexes and subnuclear organelles. For example, RNA polymerase II transcription sites are confined to discrete loci in the nucleoplasm, in which RNA polymerase II complexes and mRNA processing factors are associated. For these so called 'transcription factories' a size of 40-80 nm has been determined (Martin et al., 2004), This is similar to the size of the 464 kDa dextrans for which a striking increase in accessibility has been observed here in response to histone acetylation. Thus, it is conceivable that the relatively dense packaging in heterochromatin inhibits the formation of RNA polymerase II transcription factories in a histone acetylation-dependent manner. Furthermore, for Cajal and PML nuclear bodies, diameters between 0.1 and 1 μm have been reported, with their number and size being highly dependent on cell cycle and cell type (Gall, 2000; Zhong et al., 2000). The mobility of PML and Cajal bodies appears to be strongly dependent on the chromatin accessibility and dynamics (Görisch et al., 2005; Görisch et al., 2004), and the observed accessibility changes in heterochromatin might be relevant for the distribution of the smaller sized nuclear bodies with ~100 nm diameter and below.

In summary, the chromatin accessibility changes due to histone acetylation observed here could represent an important regulatory mechanism relevant for protein complexes in the 2-3 MDa range as well as larger supramolecular associates with 40-100 nm diameter. The chromatin decondensation due to acetylation showed a half-time $t_{1/2}$ of 210 minutes and was reversible upon removal of TSA on a similar time scale. This correlates well with the kinetics of bulk histone acetylation with $t_{1/2}$ between 200 and 400 minutes and deacetylation with $t_{1/2}$=30-150 minutes (Sun et al., 2003). Thus, global histone acetylation, chromatin decondensation and the accompanying increase of chromatin accessibility as well as their reversal occur with a half-time of several hours. However, as about 10-15% of the histones are acetylated and deacetylated with a half-time $t_{1/2}$ of about 3-8 minutes it is possible that local changes of chromatin compaction and accessibility can occur also on the minute time scale.

In mitotic cells, the chromatin was highly condensed with a general accessibility limit of 10-20 nm. For metaphase chromosomes, an average DNA concentration of 0.17 g/ml has been determined (Daban, 2003). With a nucleosome repeat length of 200 bp, this yields a nucleosome concentration of 1.3 mM. This packaging density of nucleosomes throughout the mitotic chromosomes corresponds to the 1.1-1.3 mM concentration present within the 30 nm fiber and defines the upper limit for its packaging (Daban, 2003; Weidemann et al., 2003). Accordingly, it is hardly possible for proteins or protein complexes significantly larger than a nucleosome (cylindrical shape with ~11 nm diameter and ~5.5 nm height) to intrude into metaphase chromosomes. This matches with our observation that the 77 kDa dextrans ($2R_G$ ~19 nm) are completely excluded from metaphase chromosomes, while smaller transcription factors of 10 nm in size have access (Chen et al., 2005). Remnants of this highest chromatin compaction state might at least partially persist in interphase cells and could be the origin of the densest interphase chromatin fraction, for which an apparent pore size of 16-20 nm was

calculated. However, the accessibility of dextrans to the mitotic chromosomes did not change in the presence of TSA, indicating a structural difference between the two conformations.

The HeLa cells studied here are a transformed tumor cell line and the question arises to what extend the functional implication that histone acetylation regulates the accessibility of chromatin can be generalized. Although HeLa cells have severe cytogenetic alteration (Macville et al., 1999), global changes of the interphase nuclear structure that are regarded as characteristic of cancer cells (for a review see Zink et al., 2004) are not obvious at light microscopy resolution. The chromatin distribution of HeLa cells with DNA-dense regions at the nuclear periphery, around the nucleolus and at foci in the interior of the nucleus is very similar to the chromatin density pattern seen in non-transformed human fibroblast cell lines like MRC5 (Hendzel et al., 1998) or primary human fibroblast cells (Cremer et al., 2004). Furthermore, the co-localization of DNA-dense regions, centromeres, histone tri-H3K9 and tri-H4K20 methylation and the distribution of HP1 proteins that are characteristic for heterochromatin have been reported to be similar for primary human fibroblasts and immortalized cell lines like HeLa or MCF7 (Cremer et al., 2004; Gilchrist et al., 2004; Minc et al., 1999; Zinner et al., 2005). In addition, no significant differences were observed with respect to the pattern of acetylation of lysine 9 of histone H3 and lysine 5 of histone H4 between human primary fibroblasts, transformed fibroblasts, HeLa, and HT1080 cells, which all showed a hypoacetylation at the nuclear periphery (Gilchrist et al., 2004; Sadoni et al., 1999). It is also noteworthy that the addition of TSA triggered a significant enhancement of H3 and H4 acetylation in these and other cell types (Gilchrist et al., 2004; Taddei et al., 2005; Taddei et al., 1999). Thus, the central aspects of heterochromatin studied here and the TSA-induced increase of the histone acetylation level at the nuclear periphery appear to be the same in HeLa cells and in primary human fibroblasts.

Our analysis is based on the averaged correlative evaluation of local intensity fluctuations down to the level of single pixels, with the dextrans being used as a molecular ruler with nm resolution. With this approach, information on the accessibility of chromatin structures is obtained that are smaller than the diffraction-limited resolution of the fluorescence microscope image, inasmuch as these domains change the dextran to chromatin intensity ratio. Current progress in fluorescence microscopy imaging has improved the resolution for biological samples to $\leqslant$100 nm (Hell, 2003), and numerous other fluorescent probes with defined sizes in the nm range like microspheres, quantum dots or autofluorescent proteins are available. Thus, it seems feasible to obtain a high resolution accessibility map of the nucleus, in which conformation changes on the level of the 30 nm chromatin fiber and its next folding step, the ~100 nm chromonema fiber (Belmont and Bruce, 1994), can be studied at a resolution of single genes. The DNA accessibility in these structures is a central aspect for the regulation of gene expression not only in response to histone acetylation but also to histone/DNA methylation and the effect of chromosomal proteins like linker histones, heterochromatin protein HP1 and histone variants. Accordingly, we anticipate that the approach described here will prove useful in future studies to elucidate the relation between chromatin modifying factors and chromatin conformation.

We are grateful to Cristina Cardoso, Stephanie Geiger, Stephanie Fesser and Thibaud Jegou for valuable help, and thank Marion Cremer and Roman Zinner for discussion. This work was supported by the Deutsche Forschungsgemeinschaft (grants Li406/5-3 and Ri828/5-1) and the Volkswagen Foundation in the program Junior Research Groups at German Universities.

References

Agalioti, T., Chen, G. and Thanos, D. (2002). Deciphering the transcriptional histone acetylation code for a human gene. *Cell* **111**, 381-392.

Bellard, M., Kuo, M. T., Dretzen, G. and Chambon, P. (1980). Differential nuclease sensitivity of the ovalbumin and beta-globin chromatin regions in erythrocytes and oviduct cells of laying hen. *Nucleic Acids Res.* **8**, 2737-2750.

Belmont, A. S. and Bruce, K. (1994). Visualization of G1 chromosomes: a folded, twisted, supercoiled chromonema model of interphase chromatid structure. *J. Cell Biol.* **127**, 287-302.

Chen, D., Dundr, M., Wang, C., Leung, A., Lamond, A., Misteli, T. and Huang, S. (2005). Condensed mitotic chromatin is accessible to transcription factors and chromatin structural proteins. *J. Cell Biol.* **168**, 41-54.

Chen, L. and Widom, J. (2004). Molecular basis of transcriptional silencing in budding yeast. *Biochem. Cell Biol.* **82**, 413-418.

Cremer, M., Zinner, R., Stein, S., Albiez, H., Wagler, B., Cremer, C. and Cremer, T. (2004). Three dimensional analysis of histone methylation patterns in normal and tumor cell nuclei. *Eur. J. Histochem.* **48**, 15-28.

Daban, J. R. (2003). High concentration of DNA in condensed chromatin. *Biochem. Cell Biol.* **81**, 91-99.

Dillon, N. (2004). Heterochromatin structure and function. *Biol. Cell* **96**, 631-637.

Dillon, N. and Festenstein, R. (2002). Unravelling heterochromatin: competition between positive and negative factors regulates accessibility. *Trends Genet.* **18**, 252-258.

Ekwall, K., Olsson, T., Turner, B. M., Cranston, G. and Allshire, R. C. (1997). Transient inhibition of histone deacetylation alters the structural and functional imprint at fission yeast centromeres. *Cell* **91**, 1021-1032.

Fejes Tóth, K., Knoch, T. A., Wachsmuth, M., Frank-Stöhr, M., Stöhr, M., Bacher, C. P., Müller, G. and Rippe, K. (2004). Trichostatin A-induced histone acetylation causes decondensation of interphase chromatin. *J. Cell Sci.* **117**, 4277-4287.

Gall, J. G. (2000). Cajal bodies: the first 100 years. *Annu. Rev. Cell Dev. Biol.* **16**, 273-300.

Gilbert, N., Boyle, S., Fiegler, H., Woodfine, K., Carter, N. P. and Bickmore, W. A. (2004). Chromatin architecture of the human genome: gene-rich domains are enriched in open chromatin fibers. *Cell* **118**, 555-566.

Gilchrist, S., Gilbert, N., Perry, P. and Bickmore, W. A. (2004). Nuclear organization of centromeric domains is not perturbed by inhibition of histone deacetylases. *Chromosome Res.* **12**, 505-516.

Görisch, S. M., Richter, K., Scheuermann, M. O., Herrmann, H. and Lichter, P. (2003). Diffusion-limited compartmentalization of mammalian cell nuclei assessed by microinjected macromolecules. *Exp. Cell Res.* **289**, 282-294.

Görisch, S. M., Wachsmuth, M., Ittrich, C., Bacher, C. P., Rippe, K. and Lichter, P. (2004). Nuclear body movement is determined by chromatin accessibility and dynamics. *Proc. Natl. Acad. Sci. USA* **101**, 13221-13226.

Görisch, S. M., Lichter, P. and Rippe, K. (2005). Mobility of multi-subunit complexes in the nucleus: accessibility and dynamics of chromatin subcompartments. *Histochem. Cell Biol.* **123**, 217-228.

Hassan, A. H., Prochasson, P., Neely, K. E., Galasinski, S. C., Chandy, M., Carrozza, M. J. and Workman, J. L. (2002). Function and selectivity of bromodomains in anchoring chromatin-modifying complexes to promoter nucleosomes. *Cell* **111**, 369-379.

Heitz, R. (1928). Das Heterochromatin der Moose. *Jahrb. Wiss. Botanik* **69**, 762-818.

Hell, S. W. (2003). Toward fluorescence nanoscopy. *Nat. Biotechnol.* **21**, 1347-1355.

Hendzel, M. J., Kruhlak, M. J. and Bazett-Jones, D. P. (1998). Organization of highly acetylated chromatin around sites of heterogeneous nuclear RNA accumulation. *Mol. Biol. Cell* **9**, 2491-2507.

Hoshikawa, Y., Kwon, H. J., Yoshida, M., Horinouchi, S. and Beppu, T.

(1994). Trichostatin A induces morphological changes and gelsolin expression by inhibiting histone deacetylase in human carcinoma cell lines. *Exp. Cell Res.* **214**, 189-197.

Jeppesen, P., Mitchell, A., Turner, B. and Perry, P. (1992). Antibodies to defined histone epitopes reveal variations in chromatin conformation and underacetylation of centric heterochromatin in human metaphase chromosomes. *Chromosoma* **101**, 322-332.

Jiang, G., Yang, F., Sanchez, C. and Ehrlich, M. (2004). Histone modification in constitutive heterochromatin versus unexpressed euchromatin in human cells. *J. Cell Biochem.* **93**, 286-300.

Johnson, C. A., O'Neill, L. P., Mitchell, A. and Turner, B. M. (1998). Distinctive patterns of histone H4 acetylation are associated with defined sequence elements within both heterochromatic and euchromatic regions of the human genome. *Nucleic Acids Res.* **26**, 994-1001.

Kadonaga, J. T. (1998). Eukaryotic transcription: an interlaced network of transcription factors and chromatin-modifying machines. *Cell* **92**, 307-313.

Lachner, M., O'Sullivan, R. J. and Jenuwein, T. (2003). An epigenetic road map for histone lysine methylation. *J. Cell Sci.* **116**, 2117-2124.

Lukacs, G. L., Haggie, P., Seksek, O., Lechardeur, D., Freedman, N. and Verkman, A. S. (2000). Size-dependent DNA mobility in cytoplasm and nucleus. *J. Biol. Chem.* **275**, 1625-1629.

Lénárt, P., Rabut, G., Daigle, N., Hand, A. R., Terasaki, M. and Ellenberg, J. (2003). Nuclear envelope breakdown in starfish oocytes proceeds by partial NPC disassembly followed by a rapidly spreading fenestration of nuclear membranes. *J. Cell Biol.* **160**, 1055-1068.

Macville, M., Schrock, E., Padilla-Nash, H., Keck, C., Ghadimi, B. M., Zimonjic, D., Popescu, N. and Ried, T. (1999). Comprehensive and definitive molecular cytogenetic characterization of HeLa cells by spectral karyotyping. *Cancer Res.* **59**, 141-150.

Maison, C. and Almouzni, G. (2004). HP1 and the dynamics of heterochromatin maintenance. *Nat. Rev. Mol. Cell. Biol.* **5**, 296-304.

Maison, C., Bailly, D., Peters, A. H., Quivy, J. P., Roche, D., Taddei, A., Lachner, M., Jenuwein, T. and Almouzni, G. (2002). Higher-order structure in pericentric heterochromatin involves a distinct pattern of histone modification and an RNA component. *Nat. Genet.* **30**, 329-334.

Martin, S., Failla, A. V., Spori, U., Cremer, C. and Pombo, A. (2004). Measuring the size of biological nanostructures with spatially modulated illumination microscopy. *Mol. Biol. Cell* **15**, 2449-2455.

Minc, E., Allory, Y., Worman, H. J., Courvalin, J. C. and Buendia, B. (1999). Localization and phosphorylation of HP1 proteins during the cell cycle in mammalian cells. *Chromosoma* **108**, 220-234.

Neil, K. J., Ridsdale, R. A., Rutherford, B., Taylor, L., Larson, D. E., Glibetic, M., Rothblum, L. I. and Harauz, G. (1996). Structure of recombinant rat UBF by electron image analysis and homology modelling. *Nucleic Acids Res.* **24**, 1472-1480.

Nielsen, A. L., Oulad-Abdelghani, M., Ortiz, J. A., Remboutsika, E., Chambon, P. and Losson, R. (2001). Heterochromatin formation in mammalian cells: interaction between histones and HP1 proteins. *Mol. Cell* **7**, 729-739.

Niki, T., Rombouts, K., De Bleser, P., De Smet, K., Rogiers, V., Schuppan, D., Yoshida, M., Gabbiani, G. and Geerts, A. (1999). A histone deacetylase inhibitor, trichostatin A, suppresses myofibroblastic differentiation of rat hepatic stellate cells in primary culture. *Hepatology* **29**, 858-867.

Peters, A. H. and Schubeler, D. (2005). Methylation of histones: playing memory with DNA. *Curr. Opin. Cell Biol.* **17**, 230-238.

Petersen, N. O. (2001). FCS and spatial correlations on biological surfaces. In *Fluorescence Correlation Spectroscopy–Theory and Applications* (eds R. Rigler and E. S. Elson), pp. 162-184. Heidelberg: Springer.

Rippe, K., Mücke, N. and Schulz, A. (1998). Association states of the transcription activator protein NtrC from E. coli determined by analytical ultracentrifugation. *J. Mol. Biol.* **278**, 915-933.

Roh, T. Y., Cuddapah, S. and Zhao, K. (2005). Active chromatin domains are defined by acetylation islands revealed by genome-wide mapping. *Genes Dev.* **19**, 542-552.

Sadoni, N., Langer, S., Fauth, C., Bernardi, G., Cremer, T., Turner, B. M. and Zink, D. (1999). Nuclear organization of mammalian genomes. Polar chromosome territories build up functionally distinct higher order compartments. *J. Cell Biol.* **146**, 1211-1226.

Seksek, O., Biwersi, J. and Verkman, A. S. (1997). Translational diffusion of macromolecule-sized solutes in cytoplasm and nucleus. *J. Cell Biol.* **138**, 131-142.

Smith, C. L., Horowitz-Scherer, R., Flanagan, J. F., Woodcock, C. L. and Peterson, C. L. (2003). Structural analysis of the yeast SWI/SNF chromatin remodeling complex. *Nat. Struct. Biol.* **10**, 141-145.

Strahl, B. D. and Allis, C. D. (2000). The language of covalent histone modifications. *Nature* **403**, 41-45.

Sun, J. M., Spencer, V. A., Chen, H. Y., Li, L. and Davie, J. R. (2003). Measurement of histone acetyltransferase and histone deacetylase activities and kinetics of histone acetylation. *Methods* **31**, 12-23.

Taddei, A., Roche, D., Sibarita, J. B., Turner, B. M. and Almouzni, G. (1999). Duplication and maintenance of heterochromatin domains. *J. Cell Biol.* **147**, 1153-1166.

Taddei, A., Maison, C., Roche, D. and Almouzni, G. (2001). Reversible disruption of pericentric heterochromatin and centromere function by inhibiting deacetylases. *Nat. Cell Biol.* **3**, 114-120.

Taddei, A., Roche, D., Bickmore, W. A. and Almouzni, G. (2005). The effects of histone deacetylase inhibitors on heterochromatin: implications for anticancer therapy? *EMBO Rep.* **6**, 520-524.

Tse, C., Georgieva, E. I., Ruiz-Garcia, A. B., Sendra, R. and Hansen, J. C. (1998). Gcn5p, a transcription-related histone acetyltransferase, acetylates nucleosomes and folded nucleosomal arrays in the absence of other protein subunits. *J. Biol. Chem.* **273**, 32388-32392.

Tseng, Y., Lee, J. S., Kole, T. P., Jiang, I. and Wirtz, D. (2004). Micro-organization and visco-elasticity of the interphase nucleus revealed by particle nanotracking. *J. Cell Sci.* **117**, 2159-2167.

van Holde, K. E. (1989). *Chromatin*. Heidelberg: Springer.

Verschure, P. J., van der Kraan, I., Manders, E. M., Hoogstraten, D., Houtsmuller, A. B. and van Driel, R. (2003). Condensed chromatin domains in the mammalian nucleus are accessible to large macromolecules. *EMBO Rep.* **4**, 861-866.

Weidemann, T., Wachsmuth, M., Knoch, T. A., Muller, G., Waldeck, W. and Langowski, J. (2003). Counting nucleosomes in living cells with a combination of fluorescence correlation spectroscopy and confocal imaging. *J. Mol. Biol.* **334**, 229-240.

Weintraub, H. and Groudine, M. (1976). Chromosomal subunits in active genes have an altered conformation. *Science* **193**, 848-856.

Wu, C., Wong, Y. C. and Elgin, S. C. (1979). The chromatin structure of specific genes: II. Disruption of chromatin structure during gene activity. *Cell* **16**, 807-814.

Yankulov, K., Todorov, I., Romanowski, P., Licatalosi, D., Cilli, K., McCracken, S., Laskey, R. and Bentley, D. L. (1999). MCM proteins are associated with RNA polymerase II holoenzyme. *Mol. Cell. Biol.* **19**, 6154-6163.

Zhang, W., Bone, J. R., Edmondson, D. G., Turner, B. M. and Roth, S. Y. (1998). Essential and redundant functions of histone acetylation revealed by mutation of target lysines and loss of the Gcn5p acetyltransferase. *EMBO J.* **17**, 3155-3167.

Zhong, S., Salomoni, P. and Pandolfi, P. P. (2000). The transcriptional role of PML and the nuclear body. *Nat. Cell Biol.* **2**, E85-E90.

Zimmer, C. and Wahnert, U. (1986). Nonintercalating DNA-binding ligands: specificity of the interaction and their use as tools in biophysical, biochemical and biological investigations of the genetic material. *Prog. Biophys. Mol. Biol.* **47**, 31-112.

Zink, D., Fische, A. H. and Nickerson, J. A. (2004). Nuclear structure in cancer cells. *Nat. Rev. Cancer* **4**, 677-687.

Zinner, R., Albiez, H., Walter, J., Peters, A. H., Cremer, T. and Cremer, M. (2005). Histone lysine methylation patterns in human cell types are arranged in distinct three-dimensional nuclear zones. *Histochem. Cell Biol.* doi:10.1007/s00418-005-0049-1